Construction of local coordination environment of iron sites over g-C$_3$N$_4$/PCN-222(Fe) composite with high CO$_2$ photoreduction performance

Desen Zhou [a], Xuan Zhang [a], Zheng Li [a], Jun Zhang [a,*], Tielin Wang [a,*], Shaowen Cao [b,*]

[a] Key Laboratory of Green Chemical Process of Ministry of Education, Hubei Key Laboratory of Novel Reactor and Green Chemical Technology, School of Chemical Engineering and Pharmacy, Wuhan Institute of Technology, Wuhan 430205, PR China
[b] State Key Laboratory of Advanced Technology for Materials Synthesis and Processing, Wuhan University of Technology, Wuhan 430070, PR China

ARTICLE INFO

ABSTRACT

Photocatalytic conversion of CO$_2$ to usable fuels provides a new strategy for solving energy problems and the greenhouse effect. Porphyrin-based metal-organic frameworks (MOFs) are promising in photocatalysis due to their remarkable light harvesting ability, and the metal active site and its coordination environment can be further adjusted to achieve the high activity. In this work, g-C$_3$N$_4$/PCN-222 composites with different porphyrin metal centers were fabricated and the g-C$_3$N$_4$/PCN-222(Fe^{III}) catalyst showed the highest photocatalytic CO$_2$ reduction performance than that of g-C$_3$N$_4$/PCN-222(Fe^{II}) and other g-C$_3$N$_4$/PCN-222(*M*, *M* = Co, Ni, Cu, Zn) composites. Experimental studies and theoretical calculations showed that the axial coordination in g-C$_3$N$_4$/PCN-222(Fe^{III}) distorts the square planar field (Fe-N4) to quasi-octahedral coordination, which led to the moderate adsorption ability of CO$_2$ reduction intermediate (*CO), resulting in the high photocatalytic activity.

1. Introduction

Population growth and rapid economic development have led to an increase in fossil fuel use, and the consumption of these fossil fuels is having a serious impact on the world's environment [1,2]. Photocatalysis plays a crucial role in sustainable energy development and environmental remediation [3,4]. Significantly, it is crucial to develop suitable photocatalysts to perform the catalytic process efficiently. Among various photocatalytic materials, two-dimensional graphite-phase carbon-nitrides (g-C$_3$N$_4$) have attracted much attention because of its suitable energy band structure, easily adjustable morphology, ease of synthesis and high stability [5,6]. Previous studies have found that g-C$_3$N$_4$ alone suffers from low solar light utilization and rapid compounding of photogenerated carriers, which makes its photocatalytic efficiency difficult to meet the requirements of practical applications. It should to be noted that heterojunction construction is currently a relatively simple and effective strategy to enhance the photocatalytic performance of the system [7,8], and various functional nanomaterials such as metals, oxides, sulfides, carbon-based derivatives, polymers, MOFs, covalent organic frameworks (COFs) have been successfully coupled with g-C$_3$N$_4$ and displayed the excellent photocatalytic activity [9–11].

Among various composite nanomaterials, metal-organic frameworks, as a class of crystalline organometallic materials, have received much attention as multiphase catalysts in CO$_2$ conversion reactions due to their large specific surface areas, tunable pore sizes, unique structures, catalytic properties and so on [12]. Specifically, porphyrin-based MOFs involving highly conjugated 18π-electron macrocycles are promising in photocatalysis due to their remarkable light-harvesting ability [13,14]. Moreover, the heterocyclic structure of porphyrin can serve as four-coordinated N ligands for diverse metal ions to install adsorption and/or active sites to further improve the catalytic performance [15,16]. In addition, several studies have shown that the catalytic behavior of M-N catalysts with different metal centers is following Sabatier's principle, which means that a suitable binding strength between the metal center and the reaction intermediates plays a very important role for the high activity [17,18]. In particular, Fe-N catalysts with Fe-N4 active centers are located on the strong binding side of the M-N volcano curve, indicating excellent activity and good stability [19–22]. However, the coordination environment and electronic structure of Fe center can be easily adjusted by the different chemical states of Fe [23,24], and the intrinsic mechanism for the CO$_2$ photoreduction through these porphyrin-based MOFs containing Fe metal centers should be further investigated.

Herein, PCN-222(*M*) MOFs with different metal porphyrin structures (*M*-TCPP, *M* = Co^{2+}, Ni^{2+}, Cu^{2+}, Zn^{2+}, Fe^{2+} and Fe^{3+}) were fabricated and coupled with g-C_3N_4 ultrathin nanosheets through a solvothermal method for the photocatalytic CO_2 reduction reaction. The g-C_3N_4/PCN-222(Fe^{III}) sample showed the highest CO production activity (28.5 µmol g^{-1} h^{-1}), which was much higher than that of g-C_3N_4/PCN-222(Fe^{II}) (17.6 µmol g^{-1} h^{-1}), g-C_3N_4/PCN-222(Co^{II}) (2.0 µmol g^{-1} h^{-1}) and g-C_3N_4/PCN-222(Cu^{II}) (5.6 µmol g^{-1} h^{-1}). Experimental and theoretical analyses indicate that compared with g-C_3N_4/PCN-222(Fe^{II}), the axial coordination in g-C_3N_4/PCN-222(Fe^{III}) gives the Fe center a quasi-octahedral coordination (Cl-Fe-N4) with a low spin state. The weakened spin polarization on its dz^2, dxz and dyz orbitals leads to moderate hybridization with the p orbitals of the CO_2 reduction intermediate (*CO), which greatly reduces the desorption energy barrier. Thus g-C_3N_4/PCN-222(Fe^{III}) possesses stronger intrinsic reactivity than g-C_3N_4/PCN-222(Fe^{II}).

2. Experimental

2.1. Reagents and materials

Pyrrole (Aladdin), 4-formacylmethyl benzoate (Aladdin), propionic acid (Sinopharm), potassium hydroxide (Sinopharm), tricyanic acid (Macklin), 2,4-diamino-6-methyl-1,3,5-triazine (Macklin), melamine (Sinopharm), *N*, *N*-dimethylformamide (DMF) (Sinopharm), tetrahydrofuran (Sinopharm). All chemicals used were of analytical grade and used without further purification. Distilled water was used in all experiments.

2.2. Synthesis of materials

2.2.1. Synthesis of g-C_3N_4

Ultrathin lamellar porous graphite carbon nitride (g-C_3N_4) was synthesized by supramolecular modification strategy [25]. Briefly, 8 mmol of tricyanic acid, 4 mmol of melamine and 4 mmol of 2,4-diamino-6-methyl-1,3,5-triazine were mixed in 500 mL deionized water and stirred violently for 48 h. The white solid was obtained by centrifugation and placed in an 80 °C vacuum drying oven for 24 h. Finally, the obtained white powder was transferred to a capped ceramic boat and placed in a tubular furnace. In the N_2 atmosphere, the white powder was placed in a semi-closed ceramic crucible and calcined at 550 °C for 4 h with a heating rate of 2 °C min^{-1}.

2.2.2. Synthesis of metal-tetracarboxyphenylporphyrin

Metal-tetracarboxyphenylporphyrin (*M*-TCPP) was synthesized according to the literature method [26]. Taking tetracarboxyphenyl iron porphyrin as an example, the specific steps are as follows:

(1) 3.0 g (0.043 mol) pyrrole and 6.9 g (0.042 mol) 4-formacylmethyl benzoate were dissolved in 100 mL of propionic acid, and the mixture was refluxed for 12 h at 120 °C without light and then cooled, the dark purple solid was obtained by filtration. 0.854 g (1.0 mmol) of the above purple solid and 12.8 mmol of $FeCl_3$ were dissolved in 100 mL of DMF and refluxed at 120 °C for 12 h. After cooling to room temperature, 150 mL of water was added to make the product precipitate. The solid product was obtained by filtration, washed three times with water and then dried.

(2) The solid product (0.75 g) obtained in the previous step was dissolved in 50 mL of a mixture of tetrahydrofuran and methanol (1:1, v/v), 25 mL of aqueous KOH (2.63 g) was added and refluxed at 70 °C for 12 h. The organic solvent was removed by vacuum distillation. Add a small amount of water to completely dissolve the precipitated solid, adjust the pH of the solution to 1 with 1 M HCl, leave the product to fully precipitate and then filter to obtain a brown solid, wash with water and 1 M HCl alternately until the filtrate was neutral, and dry the solid product. Metal-free TCPP, Co-TCPP, Fe(II)-TCPP, Cu-TCPP, Fe(III)-TCPP were synthesized through the above process by using different metal salts ($CoCl_2$, $CuCl_2$, $FeCl_2$ and $FeCl_3$).

2.2.3. Synthesis of PCN-222(M)

70 mg of zirconium chloride ($ZrCl_4$), 50 mg of M-TCPP, and 2700 mg of benzoic acid were dissolved in 8 mL of DMF using ultrasound. The obtained mixture was heated to 120 °C in a Teflon-lined autoclave and kept for 48 h. Then it was cooled to room temperature and further filtered.

2.2.4. Synthesis of g-C_3N_4/PCN-222(M) composites

A certain amount of g-C_3N_4 powder was dispersed in 8 mL of *N*, *N*-dimethylformamide (DMF), sonicated for 60 min, and then 70 mg of zirconium chloride ($ZrCl_4$), 50 mg of M-TCPP, and 2700 mg of benzoic acid were added to the above solution, and the mixture was transferred to an autoclave with a volume of 25 mL after continued sonication for 10 min. After heating at 120 °C for 24 h and cooling to room temperature, the solid was obtained by filtration and dried at 80 °C. Different masses of g-C_3N_4 (1.5, 3.0 and 4.5 mg) were added during the reaction (the loading amounts of PCN-222 were 2.5 wt%, 5 wt% and 10 wt%). g-C_3N_4/PCN-222, g-C_3N_4/PCN-222(Co), g-C_3N_4/PCN-222(Fe^{II}), g-C_3N_4/PCN-222(Cu), g-C_3N_4/ PCN-222(Fe^{III}) were synthesized by the above methods. To further investigate the metal contents of different g-C_3N_4/PCN(M) samples, the Inductively Coupled Plasma-Optical Emission Spectrometer (ICP-OES) tests were carried out and the results are shown in Table S1, which indicate the presence of different metal centers.

2.2.5. Photocatalytic CO_2 reduction activity

The photocatalytic activity was examined by photocatalytic reduction of CO_2 in the Labsolar-6A circulation system (Beijing Perfectlight Co., Ltd). The temperature for the reaction system was maintained at 10 °C by flowing cooling water. In a typical procedure, 50 mg of photocatalyst was dispersed in a 20 mL aqueous solution with H_2O: TEOA = 1: 1 (v/v). The above suspension was poured into a 100 mL beaker and sonicated for 15 min. Subsequently, the beaker was put into reactor. The CO_2 was produced by the reaction of 4 g of $NaHCO_3$ (introduced into the bottom of the reactor before sealing) and 10 mL of 4 M H_2SO_4 solution (introduced into the reactor by a syringe). A 300 W Xe lamp was used as the light source (Beijing Perfectlight Co., Ltd, the center light intensity is ca. 150 mW/cm^2). At every one hour, the gas mixture was extracted from the reactor, and detected by an online gas chromatograph (GC-9790II, Fuli).

3. Results and discussion

3.1. Structure and morphology characterization

Fig. 1 shows the XRD patterns of g-C_3N_4, PCN-222, PCN-222(Fe^{III}), g-C_3N_4/PCN-222 and g-C_3N_4/PCN-222(Fe^{III}) samples. As shown in Fig. 1a, the diffraction peaks of PCN-222 and PCN-222(Fe^{III}) at around 7.1° and 9.5° represent the crystal structure of PCN-222, which are consistent with the previously reported and simulated X-ray diffraction spectrum [27]. The pure g-C_3N_4 and all the prepared g-C_3N_4 composite materials show a strong peak at $2\theta = 27.6°$ corresponds to the (100) plane of g-C_3N_4, which can be attributed to the interlayer accumulation of the aromatic compounds [28]. The different g-C_3N_4/PCN-222 samples show the characteristic diffraction peaks of both PCN-222 and g-C_3N_4, which proves the successful preparation of g-C_3N_4/PCN-222 composites [29].

FT-IR analysis was further carried out to verify the fine structure of the materials [30,31]. As shown in Fig. S1. For pure g-C_3N_4, the broad absorption band at around 3420 cm^{-1} originated from the stretching vibration of N-H bonds due to the free amino groups [32]. The strong bands from 1640 to 1200 cm^{-1} can be attributed to stretching vibration mode of g-C_3N_4 heterocycles [33]. The peak at 801 cm^{-1} of g-C_3N_4 can be indexed to out-of-plane breathing vibration of s-triazine units [34]. In the case of pure PCN-222, the sharp peak at 1603 cm^{-1} belongs to the vibration of C=C in the porphyrin ring, and the peak at 1410 cm^{-1} is
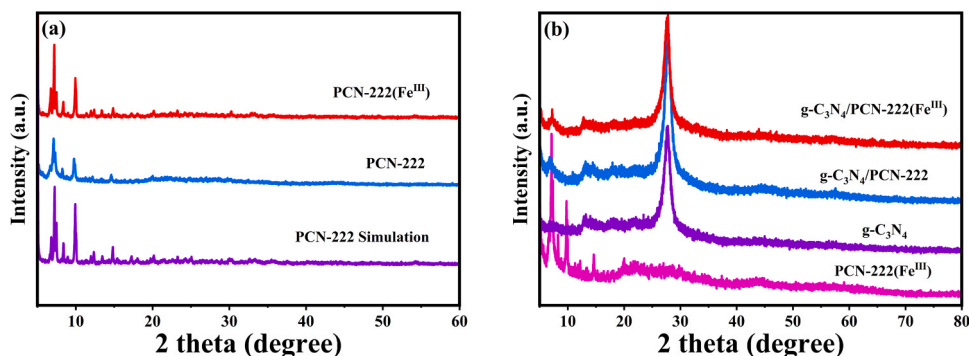
Fig. 1. XRD patterns of g-C_3N_4, PCN-222, PCN-222/g-C_3N_4 and g-C_3N_4/PCN-222(Fe^{III}).

attributed to the vibration of the C-N bond in the porphyrin ring [35]. Notably, the peaks at 998 cm^{-1} and 448 cm^{-1} belong to the stretching vibrations of Fe-N bond in metalloporphyrin and Zr-O bond in PCN-222(Fe^{III}), respectively [27]. For the g-C_3N_4/PCN-222(Fe^{III}) composite, the characteristic peaks of both PCN-222(Fe^{III}) and g-C_3N_4 can be observed, indicating the formation of heterostructures.

The morphologies of the samples were examined by scanning electron microscopy (SEM) and transmission electron microscopy (TEM). As shown in Fig. 2, g-C_3N_4 formed through supramolecular polymerization exhibited an obvious sheet-like structure (Fig. 2a) [25]. The metal-free PCN-222 shows a typical rod-like structure with several micrometers in diameter (Fig. S2) [36]. As shown in Fig. 2b, PCN-222(Fe^{III}) shows a similar morphology as metal-free PCN-222. After hybridizing, the typical morphology of g-C_3N_4/ PCN-222(Fe^{III}) composites can be seen in Fig. 2c and d, the PCN-222(Fe^{III}) microrods are wrapped by numerous

g-C_3N_4 nanosheets. This result further testifies that the composite has formed a tight heterojunction between g-C_3N_4 and PCN-222(Fe^{III}). The elemental mapping results shown in Fig. 2e illustrate the distinct distribution of C, N, O, Zr and Fe elements, which further confirms the binary nature of g-C_3N_4 and PCN-222(Fe^{III}) in the g-C_3N_4/ PCN-222 (Fe^{III}) sample.

The XPS test was used to measure the surface composition and chemical state of the photocatalysts [37,38]. The XPS spectrum of C 1 s in pure g-C_3N_4 (Fig. 3a) exhibited two peaks at 284.8 eV and 288.1 eV, which aligned with C-C bond or pure g-C_3N_4 sp^2 surface adventitious carbon and N = C-N in the g-C_3N_4 lattice, respectively [39]. Two peaks could be observed at 284.8 eV and 288.8 eV for PCN-222(Fe^{III}), which can be attributed to C-C or exogenous carbon and C=O, respectively [40]. Furthermore, the N 1 s spectra are shown in Fig. 3b, the peaks at 398.7 eV and 400.5 eV are attributed to the sp^2-hybridized N (C=N-C)
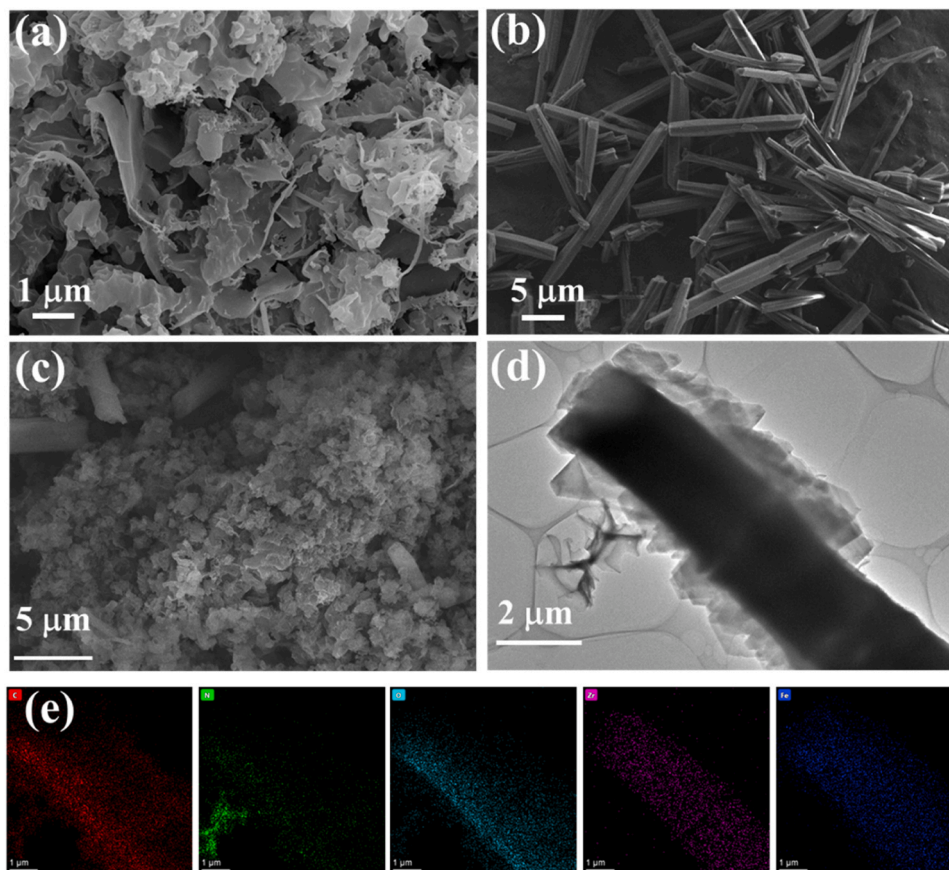

Fig. 2. SEM images of g-C_3N_4 (a), PCN-222(Fe^{III}) (b), g-C_3N_4/PCN-222(Fe^{III}) (c), TEM images of g-C_3N_4/PCN-222(Fe^{III}) (d), and the corresponding EDS element mappings of g-C_3N_4/PCN-222(Fe^{III}) (e).
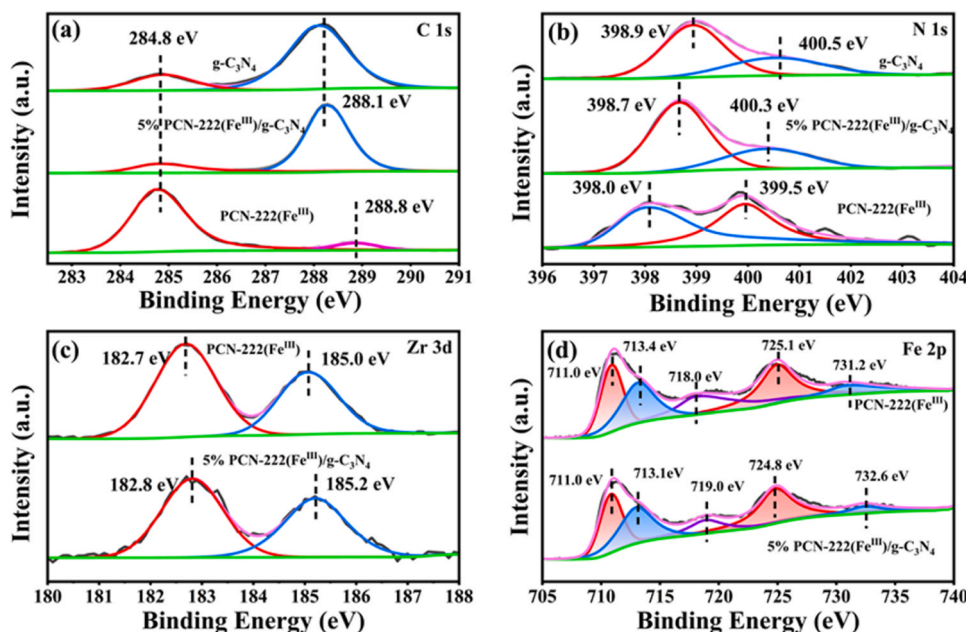
Fig. 3. High-resolution XPS spectra of (a) C 1 s, (b) N 1 s, (c) Zr 3d, (d) Fe 2p over different samples.

and the tertiary nitrogen in N-(C)$_3$ group [41]. After coupling g-C$_3$N$_4$ with PCN-222(Fe^{III}), the C═N-C binding energy of g-C$_3$N$_4$/PCN-222 (Fe^{III}) is slightly negatively shifted (about 0.2 eV), which indicates the existence of strong interaction between g-C$_3$N$_4$ and PCN-222(Fe^{III}). These results demonstrate the electron transfer from PCN-222(Fe^{III}) to g-C$_3$N$_4$ in the composite. As for the Zr 3d binding energy (Fig. 3c), pure PCN-222(Fe^{III}) and g-C$_3$N$_4$/PCN-222(Fe^{III}) are quite similar, the two strong peaks of Zr 3d at 182.7 and 150 eV can be indexed to the Zr 3d$_{5/2}$ and Zr 3d$_{3/2}$ of Zr-O cluster, respectively [42]. The high-resolution Fe 2p spectra of PCN-222(Fe^{III}) and g-C$_3$N$_4$/PCN-222(Fe^{III}) were concluded in Fig. 3d, and the typical peaks at 711.0 and 724.0 eV corresponded to Fe 2p3/2 and Fe 2p1/2, respectively [43,44]. These two peaks could be fitted to several peaks at 711.0 and 725.1 eV normally assigning to the existence of Fe^{3+}, and another peak centered at 718.0 eV can be indexed to the satellite peak of Fe^{3+}, these results indicate that Fe^{3+} is successfully embedded into the porphyrin center [45]. Fig. S3 and Table S2 show the BET surface areas, pore volumes and pore diameters of the prepared samples. The surface areas of g-C$_3$N$_4$/PCN-222 composite exhibit a high surface area (88.6 m^2 g^{-1}) due to the introduction of PCN-222. However, the g-C$_3$N$_4$/PCN-222(Fe^{III}) sample shows a decrease in surface area compared with g-C$_3$N$_4$/PCN-222, which can be attributed to the presence of metal center Fe^{III} [46].

3.2. Optical properties and band structures

The optical properties of g-C$_3$N$_4$, PCN-222 (Fe^{II}, Fe^{III} and metal-free) and g-C$_3$N$_4$/PCN-222 (Fe^{II}, Fe^{III} and metal-free) composites were tested using a UV-Vis DRS instrument. As shown in Fig. 4 and Fig. S4, the pure PCN-222 samples (Fe^{II}, Fe^{III} and metal-free) all exhibit strong absorption peaks between 200 and 800 nm due to the characteristic absorption of porphyrin compounds in the ultraviolet to visible light region [47]. The strong peak near 400–500 nm is the Soret band, and the several absorption peaks in the range of 500–700 nm can be attributed to the Q bands [29]. Significantly, their bandgaps also slightly change by the valence state of Fe (Fig. S4b). As shown in Fig. S4, the composite sample reveal strong absorption in UV and visible light region. In addition, the valence band (VB) positions of g-C$_3$N$_4$ and PCN-222 (Fe^{III}) were measured using XPS valence spectra, and the results are shown in Fig. S5. The VB positions of g-C$_3$N$_4$ and PCN-222 (Fe^{III}) are calculated to be 1.56 eV and 1.01 eV, respectively. The outcomes prove that the metal
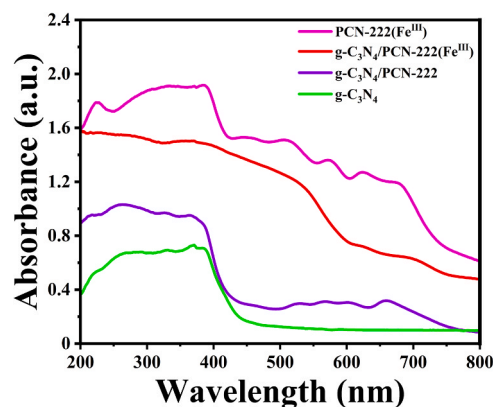

Fig. 4. UV–vis DRS of g-C$_3$N$_4$, g-C$_3$N$_4$/PCN-222, g-C$_3$N$_4$/PCN-222(Fe^{III}), PCN-222(Fe^{III}) samples.

center of the ligand can adjust the band gap structure.

3.3. Photocatalytic activity

The photocatalytic performance of all samples was tested in 3 h with a full-spectrum Xenon lamp. Control experiments confirmed that CO was not detected in the absence of a photocatalyst, CO$_2$ source or light irradiation. (Fig. S6). As shown in Figs. 5a, 5 wt% of PCN-222(Fe^{III}) in g-C$_3$N$_4$/PCN-222(Fe^{III}) composite sample exhibits the highest CO$_2$ reduction activity, and the CO production rate reaches 28.5 µmol g^{-1} h^{-1}. Furthermore, the photocatalytic performances of different g-C$_3$N$_4$/PCN-222(M) composites with the same PCN-222(M) loading content (5 wt%) were also investigated and shown in Fig. S7. Compared to pure g-C$_3$N$_4$, all the g-C$_3$N$_4$/PCN-222(*M*) samples show a substantial improvement in the performance. However, g-C$_3$N$_4$/PCN-222(Cu), g-C$_3$N$_4$/PCN-222(Ni) and g-C$_3$N$_4$/PCN-222(Co) samples exhibit lower activity compared with metal-free g-C$_3$N$_4$/PCN-222. In contrast, g-C$_3$N$_4$/PCN-222(Zn), g-C$_3$N$_4$/PCN-222(Fe^{II}) and g-C$_3$N$_4$/PCN-222(Fe^{III}) show higher CO production activity and the highest performance can be observed over g-C$_3$N$_4$/PCN-222(Fe^{III}) sample, which is about 6.8 times higher than that of pure g-C$_3$N$_4$. Such results indicate that the metal
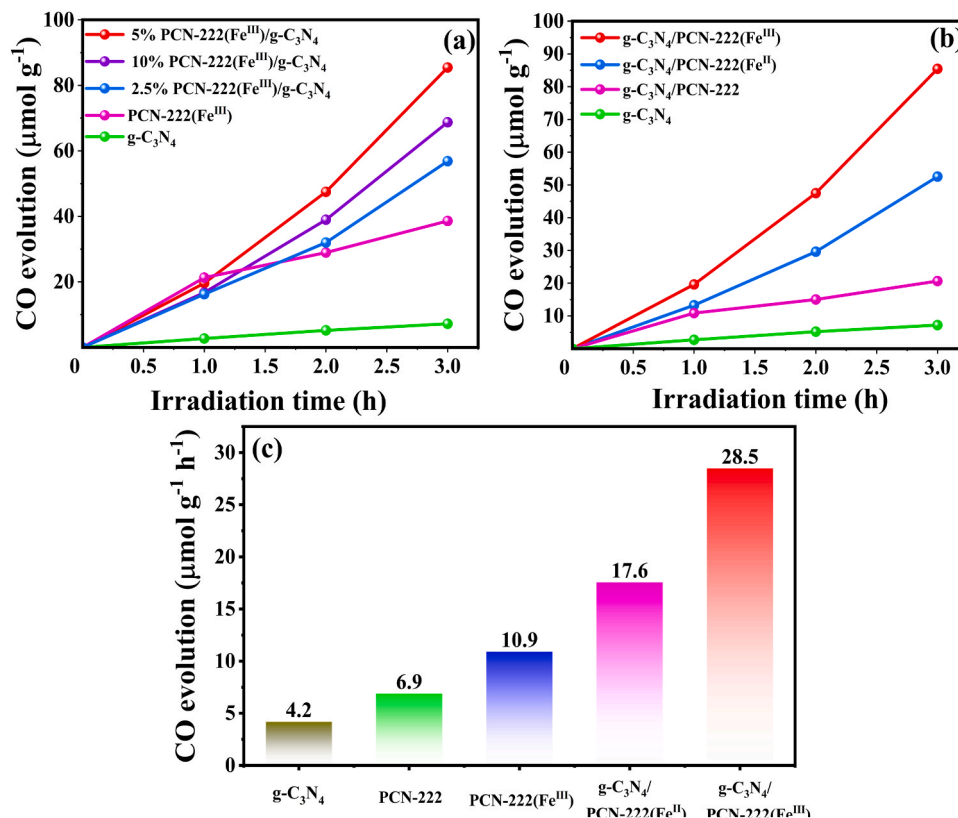
Fig. 5. Comparison of the photocatalytic performance of different samples.

center of trivalent iron in g-C$_3$N$_4$/PCN-222(Fe^{III}) plays a very important role for the high photocatalytic CO$_2$ reduction activity. In addition, as shown in Table S3 and Fig. S8, the g-C$_3$N$_4$/PCN-222(Fe^{III}) sample also exhibited the highest CO selectivity and catalyst turnover number (TON). The photocatalytic stability of g-C$_3$N$_4$/PCN-222(Fe^{III}) is also

tested for several consecutive cycles (Fig. S9), no obvious loss of activity can be detected. Furthermore, the phase structure of g-C$_3$N$_4$/PCN-222 (Fe^{III}) also showed no noticeable change after photocatalytic reaction for 9 h (Fig. S10), which verifies that the prepared photocatalyst is stable. More importantly, as shown in Fig. 6 and S11, to identify the generation
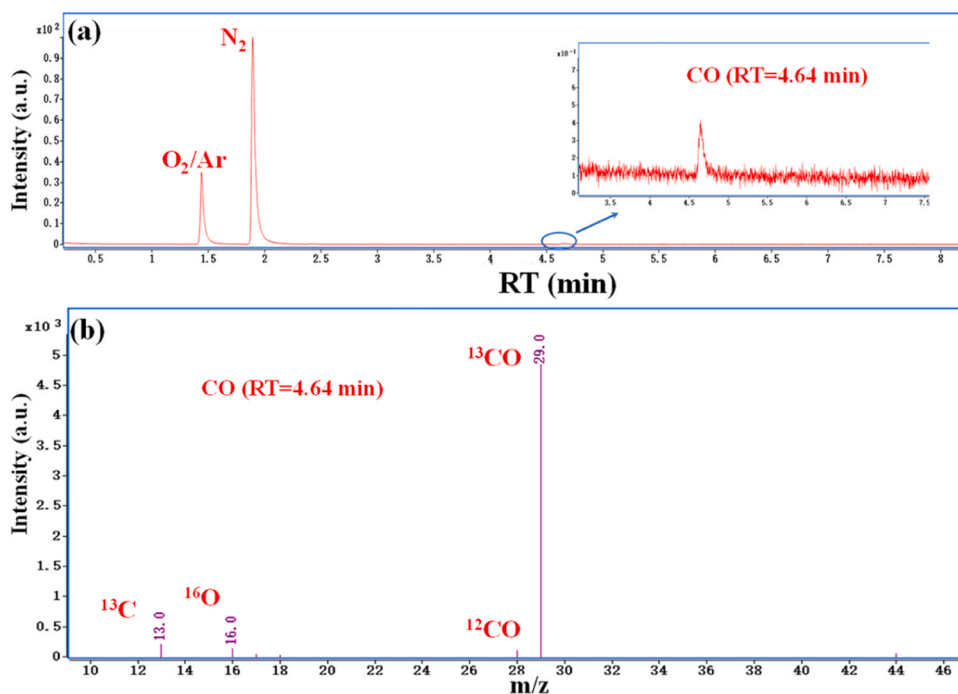

Fig. 6. (a) Total ion chromatography and (b) mass spectra of ^{13}CO over g-C$_3$N$_4$/PCN-222(Fe^{III}) in the photocatalytic reduction of ^{13}CO$_2$ under light irradiation for 3 h.

of CO originating from the input CO_2, high-purity isotope-labeled carbon dioxide ($^{13}CO_2$) was employed as a substitute source gas to evaluate the photoreduction of CO_2 over g-C_3N_4/PCN-222(Fe^{III}) sample. The peaks observed in the total ion chromatography at 4.6 min can be assigned to CO. The dominant and fragmented peaks in the corresponding mass spectra are highly consistent with those reported in the literature for CO, confirming that the products indeed derive from $^{13}CO_2$ [48,49]. Furthermore, the apparent quantum yield (AQY) of g-C_3N_4/PCN-222(Fe^{III}) composite sample under the different wavelengths of the monochromatic light are shown in Fig. S12 and Table S4. It can be seen that the g-C_3N_4/PCN-222(Fe^{III}) sample exhibits a broad-spectrum response, and the AQY$_{CO}$ is calculated to be 0.28%, 0.14%, 0.11%, 0.05% and 0.07% at 380, 420, 500, 600 and 650 nm, respectively. Table S5 lists the photocatalytic CO_2 reduction performances of recent studies on different MOFs/g-C_3N_4 composites, and the prepared g-C_3N_4/PCN-222(Fe^{III}) sample in this work represents one of the most highly effective systems.

3.4. Photoelectric properties

Photoluminescence (PL) measurements are an effective method to evaluate the separation efficiency of photogenerated charge carriers [50]. Fig. 7 shows the room temperature PL spectra of different samples under the excitation wavelength of 370 nm. As shown in Fig. 7a, the PCN-222(Fe^{III}) sample shows the lower PL intensity which demonstrates that the presence of Fe^{III} accelerates the separation of photogenerated carriers of PCN-222. The photogenerated carrier recombination rates of g-C_3N_4, g-C_3N_4/PCN-222, g-C_3N_4/PCN-222(Fe^{II}) and g-C_3N_4/PCN-222 (Fe^{III}) were also characterized and shown in Fig. 7b. The g-C_3N_4/PCN-222(Fe^{III}) sample shows the lowest PL intensity, indicating the best separation ability of photogenerated charge carriers. Besides, as displayed in Fig. 7c, the g-C_3N_4/PCN-222(Fe^{III}) composite shows the smallest arc radius, suggesting that the presence of Fe^{III} metal center can be beneficial to lower the interface resistances for charge transfer, which is more favorable to the photocatalytic reactions. Meanwhile, as shown

in Fig. 7d, the g-C_3N_4/PCN-222(Fe^{III}) sample exhibits the highest photocurrent density, further implying the best separation efficient of the photogenerated electrons and holes.

3.5. Mechanism of photogenerated charge carrier transfer

In order to reveal the photocatalytic reaction mechanism, the electron transfer between g-C_3N_4 and PCN-222(Fe^{III}) was investigated first. As shown in Fig. 8a, the work functions (Φ) of g-C_3N_4 and PCN-222(Fe^{III}) were measured to be 3.07 and 2.31 eV from ultraviolet photoemission spectroscopy (UPS), indicating that the Fermi level (E_F) of g-C_3N_4 is lower than that of PCN-222(Fe^{III}) (Fig. 8b). In this case when g-C_3N_4 intimately contacts with PCN-222(Fe^{III}), the electrons in PCN-222(Fe^{III}) will spontaneously flow to g-C_3N_4 until the Fermi levels become equal, which is also consistent with the XPS results (Fig. 4b). As a result, a robust internal electric field (IEF) can be established, directing from PCN-222(Fe^{III}) to g-C_3N_4 [51,52]. Meanwhile, the band edge of g-C_3N_4 would bend downward due to the acceptance of electrons and the band edge of PCN-222(Fe^{III}) would bend upward owing to the loss of electrons. Consequently, under the light irradiation, the electrons will be excited to the conduction band (CB) of both PCN-222(Fe^{III}) and g-C_3N_4. Driven by the interfacial IEF and the interfacial bend edge bending, the photogenerated electrons in the CB of g-C_3N_4 can be effectively transferred to PCN-222(Fe^{III}), thus greatly promoting the separation of photoinduced electrons and holes. Such electron flow can be also confirmed through in situ XPS, as shown in Fig. 8c and d, the XPS patterns of g-C_3N_4/PCN-222(Fe^{III}) were characterized in the dark and light cases, respectively. It can be seen clearly that the N 1 s binding energy of the composite sample decreases under the light irradiation, while the Zr 3d binding energy shifts positively. These results demonstrate the transfer of photogenerated electrons from g-C_3N_4 to PCN-222(Fe^{III}) under the light irradiation.

To further investigate the flow destination of photogenerated electrons over PCN-222(Fe^{III}), the charge density difference calculations were performed for Zr and Fe sites in PCN-222(Fe^{III}), and the results are
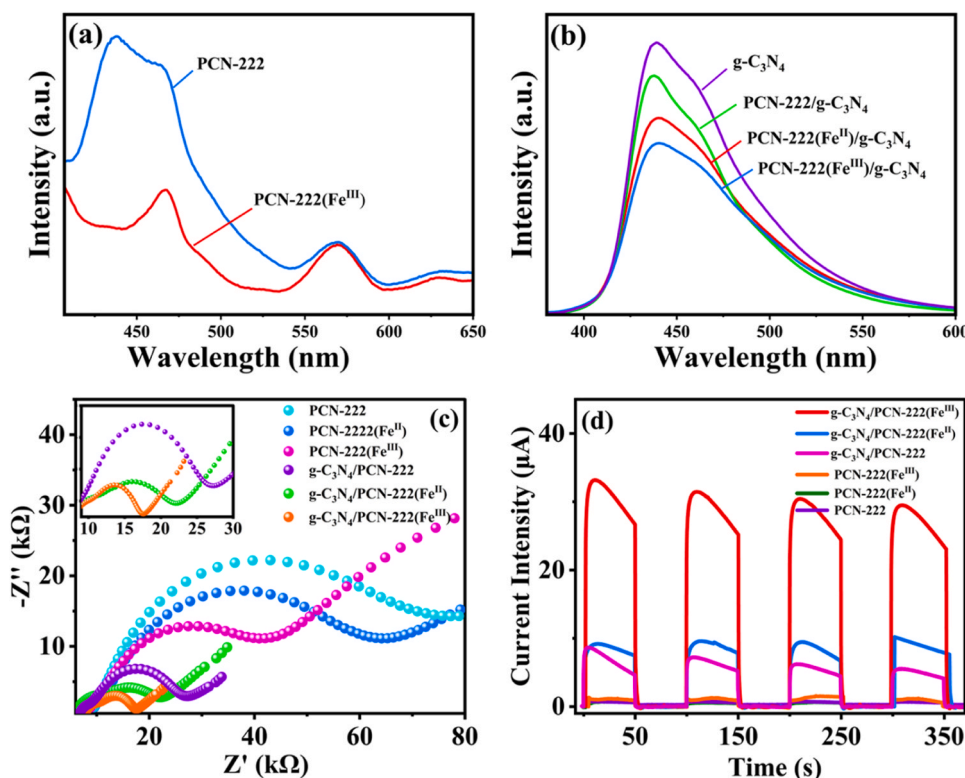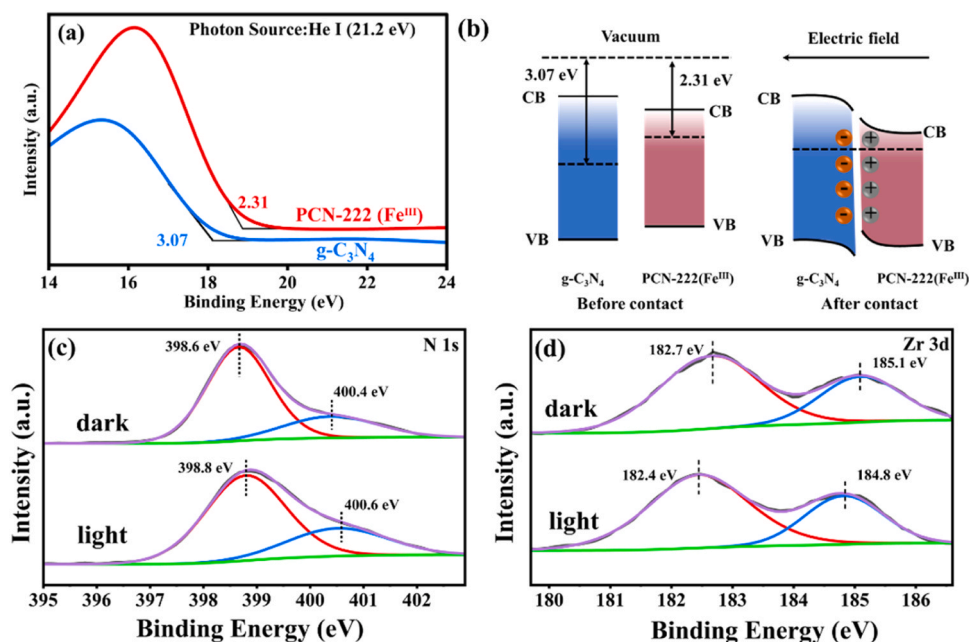

Fig. 7. (a) and (b) PL spectra, EIS spectra (c) and photocurrent density curves (d) of different samples.

Fig. 8. (a) UPS spectra of g-C_3N_4 and PCN-222(Fe^{III}), (b) schematic illustration of charge transfer process, in situ analysis of N1s (c) and Zr 3d (d) in g-C_3N_4/PCN-222 (Fe^{III}) composite samples under illumination.

shown in Fig. 9. The Bader charge analysis shows that Zr atom is more likely to lose electrons relative to Fe atom which may be due to the difference of the electronegativity. The electronegativity of Zr (1.33) is less than that of Fe (1.83), which means that the Fe sites are more likely to capture photogenerated electrons under light irradiation and become the active center for CO_2 reduction. Thus, it is very important to investigate the adsorption/desorption ability of reactants/intermediates over Fe active sites during the photocatalytic CO_2 reduction process. As shown in Fig. 10, based on the experimental conditions, PCN-222(Fe^{III}) was constructed by attaching chlorine atoms to the metallic iron center of PCN-222(Fe^{II}), the CO_2 reduction reaction processes of PCN-222(Fe^{III}) and PCN-222(Fe^{II}) were modeled optimally and the Gibbs free energy (G) was calculated for each reaction step. Firstly, the Fe^{III} and Fe^{II} sites exhibit a similar ΔG for CO_2 adsorption. The rate-determining step (RDS) over PCN-222(Fe^{II}) is the *CO desorption step with a high ΔG of 1.81 eV. However, for PCN-222(Fe^{III}), the desorption of CO becomes much easier and ΔG reduces to 0.41 eV. The RDS over PCN-222(Fe^{III}) is the *COOH formation step with a ΔG of 0.99 eV. These results clearly illustrate that Fe^{III} site could greatly lower the energy barrier for *CO desorption during the photocatalytic CO_2 reduction reaction, thus promoting the subsequent CO production activity.

To further understand the high adsorption/desorption ability of Fe^{III} and offer a better insight into the underlying regulatory mechanisms of Fe 3d electronic structure, the local electron configuration was examined through the projected density of state (PDOS) calculations

(Fig. 11a). The Fe 3d PDOS of PCN-222(Fe^{II}) reveals the asymmetric arrangement of each d-orbital electron in both spin channels, signifying the distinct spin polarization. Nevertheless, weaker spin polarization is noted in the Fe d-orbitall over PCN-222(Fe^{III}). The diminished spin polarization could be attributed to the reordering of the d-orbital energy level. Further insights into the d-orbital splitting manner were gained by the comprehensive analysis of orbital occupation and energy level based on the crystal field theory [53]. The coordination environment of PCN-222(Fe^{II}) features a D_{4h} symmetry in the square-planar field in which the five 3d orbitals of Fe split into four states: dx^2-y^2, dz^2, dxz/dyz (twofold degenerate), and dxy [54]. For PCN-222(Fe^{III}), the orbital splitting energy decreases and the dz^2 orbital energy level increases due to the electron repulsion of the axial coordination, forming a double condensed e_g orbital (dz^2 and dx^2-y^2). The electron localization function similarly shows that significant charge polarization and electron symmetry distortion are observed in PCN-222(Fe^{III}) under axial traction, showing characteristic quasi-octahedral coordination (Fig. 11b). As a result, some of the electrons in the elevated dz^2 orbital spill over to dxz/dyz orbitals, resulting in a decrease in the number of unpaired electrons in both dxz/dyz and dz^2 orbitals. The energy levels of dxz/dyz orbitals are then shifted down to form triplet simplicial states (dxz, dyz, and dxy) with t_{2g} symmetry. The axial coordination leads to a shift in the crystal field and local symmetry, from a square planar field with D_{4h} symmetry to a quasi-octahedral field with C_{4V} symmetry (Fig. 11c). Interestingly, this d-orbital configuration with a lower density of
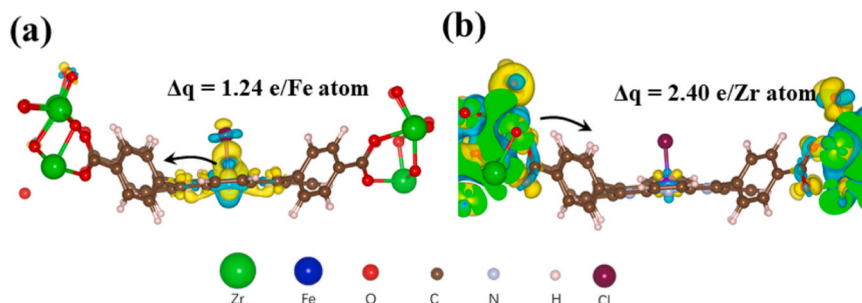
Fig. 9. Side view of the charge density difference of the PCN-222-Fe site and PCN-222-Zr site with an isosurface.
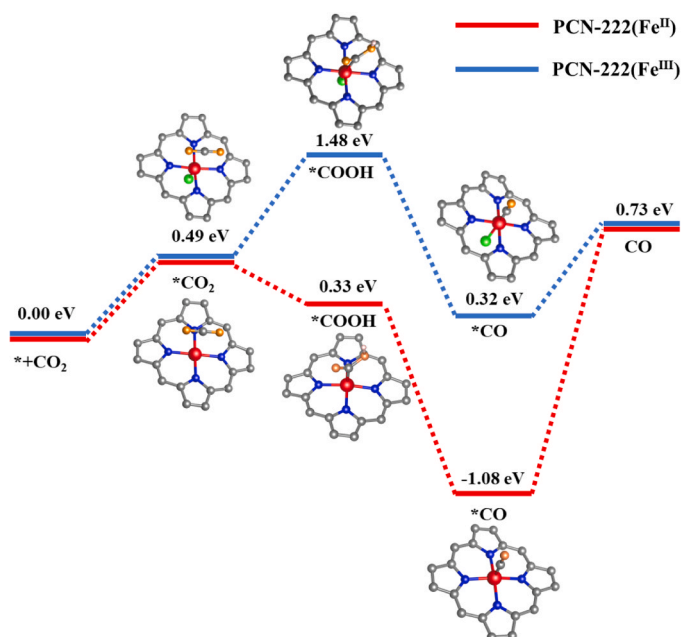
Fig. 10. Calculated Gibbs free energy diagrams of CO_2 reduction processes over the PCN-222(Fe^{II}) and PCN-222(Fe^{III}).
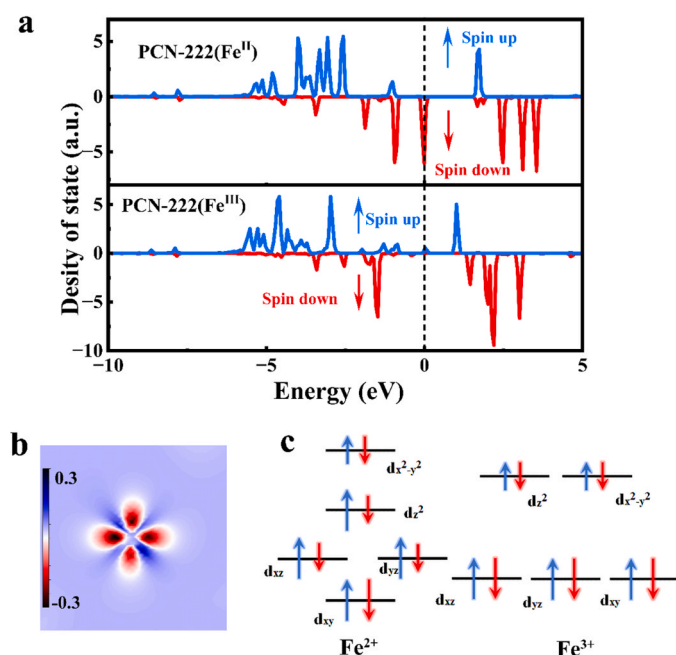

Fig. 11. (a) PDOS of Fe for PCN-222(Fe^{II}) and PCN-222(Fe^{III}), (b) electron localization functions of PCN-222(Fe^{III}) and (c) schematic diagram of the modulation of d-orbital splitting manner.

unpaired electrons on the frontal orbitals (dxz, dyz and dz^2) can confer a moderate binding strength to the intermediates of CO_2 reduction, leading to promote the progress of the reactions [55,56].

According to the above discussions, the photocatalytic CO_2 reduction mechanism of the g-C$_3$N$_4$/PCN-222(Fe^{III}) composite was proposed and shown in Fig. 12. Under the equilibrium state, the interfacial IEF can be formed due to the difference of the Fermi levels of g-C$_3$N$_4$ and PCN-222 (Fe^{III}), and the electric field direction of from PCN-222(Fe^{III}) to g-C$_3$N$_4$. Under light irradiation, the VB electrons of g-C$_3$N$_4$ and PCN-222(Fe^{III}) can be excited to CB. Driven by the interfacial IEF, the photogenerated
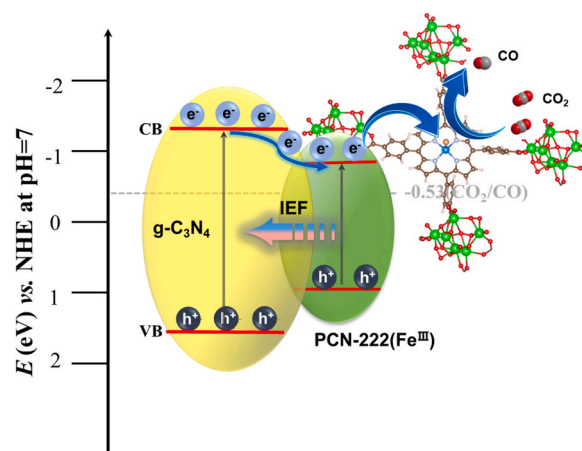

Fig. 12. Charge transfer mechanism of g-C$_3$N$_4$/PCN-222(Fe^{III}) composite.

electrons generated from g-C$_3$N$_4$ can be effectively transferred to the CB of PCN-222(Fe^{III}), which was proved by the above in situ XPS results. Importantly, the Fe^{III} site could act as the enrichment center of the photoinduced electron as well as the active center for CO_2 adsorption. Moreover, the d-orbital configuration of Fe^{III} with lower unpaired electron density can give a moderate binding strength to the reduction intermediate, which facilitates CO desorption and greatly enhances photocatalytic activity. On the other hand, photogenerated holes can be assembled in the VB of g-C$_3$N$_4$/PCN-222(Fe^{III}) and consumed by TEOA.

4. Conclusions

In summary, g-C$_3$N$_4$/PCN-222 composites with different porphyrin metal centers were fabricated by a hydrothermal method, the g-C$_3$N$_4$/PCN-222(Fe^{III}) composite exhibited the highest CO_2 photoreduction activity. The combination of density functional theory calculations and comprehensive ex situ and in situ characterization showed that the photogenerated electrons could be effectively transferred from g-C$_3$N$_4$ to PCN-222(Fe^{III}), and finally enriched on the Fe sites. Moreover, compared to the square planar coordination of g-C$_3$N$_4$/PCN-222(Fe^{II}), the axial interaction of trivalent Fe in PCN-222(Fe^{III}) allowed it to possess quasi-octahedral coordination with low spin states, leading to the reduction in the number of unpaired electrons on dz^2, dxz, and dyz orbitals, resulting in a moderate adsorption/desorption energy of the reaction intermediates of CO_2 reduction. Therefore, the g-C$_3$N$_4$/PCN-222(Fe^{III}) sample exhibited excellent CO_2 reduction activity. This work provides an important guideline for the rational construction of the coordination environment for the metal center in MOFs to modulate the catalyst performance.

CRediT authorship contribution statement

Zhou Desen: Data curation, Formal analysis, Investigation, Methodology, Writing – original draft. **Zhang Xuan:** Data curation, Writing – review & editing. **Li Zheng:** Data curation. **Zhang Jun:** Formal analysis, Funding acquisition, Resources, Writing – review & editing. **Wang Tielin:** Data curation, Funding acquisition, Supervision. **Cao Shaowen:** Formal analysis, Funding acquisition, Project administration, Writing – review & editing.

Declaration of Competing Interest

The authors declare that they have no known competing financial interests or personal relationships that could have appeared to influence the work reported in this paper.

Data Availability

Data will be made available on request.

Acknowledgments

Appendix A. Supporting information

Supplementary data associated with this article can be found in the online version at doi:10.1016/j.apcatb.2023.123639.

References

[1] A. Hayat, M. Sohail, T.A. Taha, A.M. Alenad, I. Uddin, A. Hayat, T. Ali, R. Shah, A. Irfan, W.U. Khan, A superficial intramolecular alignment of carbon nitride through conjugated monomer for optimized photocatalytic CO_2 reduction, Catalysts 11 (2021) 935.

[2] M. Sohail, T. Altalhi, A.G. Al-Sehemi, T.A.M. Taha, K.S. El-Nasser, A.A. Al-Ghamdi, M. Boukhari, A. Palamanit, A. Hayat, M. A Amin, Nanostructure engineering via intramolecular construction of carbon nitride as efficient photocatalyst for CO_2 reduction, Nanomaterials 11 (2021) 3245.

[3] H.J.W. Li, H.M. Zhou, K.J. Chen, K. Liu, S. Li, K.X. Jiang, W.H. Zhang, Y.B. Xie, Z. Cao, H.M. Li, H. Liu, X.W. Xu, H. Pan, J.H. Hu, D.S. Tang, X.Q. Qiu, J.W. Fu, M. Liu, Metallic MoO_2-Modified Graphitic Carbon Nitride Boosting Photocatalytic CO_2 Reduction via Schottky Junction, Sol. Rrl 4 (2020), 1900416.

[4] H. Zhong, R. Sa, H. Lv, S. Yang, D. Yuan, X. Wang, R. Wang, Covalent Organic Framework Hosting Metalloporphyrin-based carbon dots for visible-light-driven selective CO_2 reduction, Adv. Funct. Mater. 30 (2020), 2002654.

[5] F. Raziq, J.X. He, J.T. Gan, M. Humayun, M.B. Faheem, A. Iqbal, A. Hayat, S. Fazal, J.B. Yi, Y. Zhao, K. Dhanabalan, X.Q. Wu, A. Mavlonov, T. Ali, F. Hassan, X. Xiang, X.T. Zu, H.H. Shen, S.A. Li, L. Qiao, Promoting visible-light photocatalytic activities for carbon nitride based 0D/2D/2D hybrid system: Beyond the conventional 4-electron mechanism, Appl. Catal. B: Environ. 270 (2020), 118870.

[6] B. Kim, D. Kwon, J.-O. Baeg, M. Austeria P, G.H. Gu, J.-H. Lee, J. Jeong, W. Kim, W. Choi, Dual-Atom-Site Sn-Cu/C_3N_4 Photocatalyst selectively produces formaldehyde from CO_2 reduction, Adv. Funct. Mater. 33 (2023), 2212453.

[7] Y. Li, B.H. Li, D.N. Zhang, L. Cheng, Q.J. Xiang, Crystalline carbon nitride supported copper single atoms for photocatalytic CO_2 Reduction with nearly 100% CO selectivity, ACS Nano 14 (2020) 10552–10561.

[8] P.K. Prajapati, D. Tripathi, M.K. Poddar, P. Gupta, S.L. Jain, Dual photocatalysis for CO_2 reduction along with the oxidative coupling of benzylamines promoted by Cu/$Cu_2O@g$-C_3N_4 under visible irradiation, Sustain. Energy Fuels 6 (2022) 2996–3007.

[9] S. Wan, J. Xu, S. Cao, J. Yu, Promoting intramolecular charge transfer of graphitic carbon nitride by donor–acceptor modulation for visible-light photocatalytic H_2 evolution, Interdiscip. Mater. 1 (2022) 294–308.

[10] L.Q. Bai, H.W. Huang, S.X. Yu, D.Y. Zhang, H.T. Huang, Y.H. Zhang, Role of transition metal oxides in g-C_3N_4-based heterojunctions for photocatalysis and supercapacitors, J. Energy Chem. 64 (2022) 214–235.

[11] C. Han, X. Zhang, S. Huang, Y. Hu, Z. Yang, T.-T. Li, Q. Li, J. Qian, MOF-on-MOF-Derived Hollow Co_3O_4/In_2O_3 Nanostructure for Efficient Photocatalytic CO_2 Reduction, Advanced, Science (2023), 2300797.

[12] J.D. Xiao R. Li H.L. Jiang Met. -Org. Framew. -Based Photocatal. Sol. fuel Prod., small Methods 7 2023 2201258.

[13] S.J. Xie, Y.F. Li, B. Sheng, W.Y. Zhang, W. Wang, C.C. Chen, J.K. Li, H. Sheng, J. C. Zhao, Self-reconstruction of paddle-wheel copper-node to facilitate the photocatalytic CO_2 reduction to ethane, Appl. Catal. B: Environ. 310 (2022), 121320.

[14] R. Hariri, S. Dehghanpour, Effective visible-light CO_2 photoreduction over (metallo)porphyrin-based metal-organic frameworks to achieve useful hydrocarbons, Appl. Organomet. Chem. 35 (2021), e6422.

[15] G.X. Zhao, H. Pang, G.G. Liu, P. Li, H.M. Liu, H.B. Zhang, L. Shi, J.H. Ye, Co-porphyrin/carbon nitride hybrids for improved photocatalytic CO_2 reduction under visible light, Appl. Catal. B: Environ. 200 (2017) 141–149.

[16] J.Y. Li, Y.X. Hou, C.X. Cui, X.P. Zhang, J.C. Wang, A.R. Wang, Z.P. Chen, M.C. Li, T. J. Lou, Porphyrin-based conjugated organic polymer with dual metal sites for highly active and selective visible-light-driven reduction of CO_2 to CO, Dalton Trans. 51 (2022) 15022–15030.

[17] C.X. Zhao B.Q. Li J.N. Liu Q. Zhang Intrinsic Electro Act. Regul. M-N. -C. Single Catal. Oxyg. Reduct. React., Angew. Chem. Int. Ed. 60 2021 4448 4463.

[18] Z. Gao, H.P. Yang, J.T. Mao, J.M. Wu, Construction of alpha-Fe_2O_3 and Fe/Co-N4 structures with faceted TiO_2 nanocrystals for highly efficient degradation of sulfathiazole in water, J. Clean. Prod. 220 (2019) 668–676.

[19] F. Mo, C. Song, Q. Zhou, W. Xue, S. Ouyang, Q. Wang, Z. Hou, S. Wang, J. Wang, The optimized Fenton-like activity of Fe single-atom sites by Fe atomic clusters-

[20] mediated electronic configuration modulation, Proc. Natl. Acad. Sci. USA 120 (2023), e2300281120.

[20] C. Liu, H. Dai, C. Tan, Q. Pan, F. Hu, X. Peng, Photo-Fenton degradation of tetracycline over Z-scheme Fe-g-C_3N_4/Bi_2WO_6 heterojunctions: Mechanism insight, degradation pathways and DFT calculation, Appl. Catal. B: Environ. 310 (2022), 121326.

[21] F. Chen, X.-L. Wu, C. Shi, H. Lin, J. Chen, Y. Shi, S. Wang, X. Duan, Molecular engineering toward pyrrolic n-rich M-N4 (M = Cr, Mn, Fe, Co, Cu) single-atom sites for enhanced heterogeneous fenton-like reaction, Adv. Funct. Mater. 31 (2021), 2007877.

[22] R.N. Zhan, Y.F. Zhou, C. Liu, X.J. Wang, X.L. Sun, Y.Q. Zhu, J.F. Niu, Insights into mechanism of Fe-dominated active sites via phosphorus bridging in Fe-Ni bimetal single atom photocatalysts, Sep. Purif. Technol. 286 (2022), 120443.

[23] X.N. Zhang, X.J. Ma, Y.Q. Ye, C.X. Guo, X.J. Xu, J.W. Zhou, B. Wang, Enhanced photocatalytic hydrogen evolution with a Mixed-Valence iron Metal-Organic framework, Chem. Eng. J. 456 (2023), 140939.

[24] M. Zhao, T.L. Guo, W. Qian, Z. Wang, X. Zhao, L.L. Wen, D.P. He, Fe-incorporated cobalt-based metal-organic framework ultrathin nanosheets for electrocatalytic oxygen evolution, Chem. Eng. J. 422 (2021) 10055.

[25] Y. Wang, W. Zhen, Y. Zeng, S. Wan, H. Guo, S. Zhang, Q. Zhong, In situ self-assembly of zirconium metal-organic frameworks onto ultrathin carbon nitride for enhanced visible light-driven conversion of CO_2 to CO, J. Mater. Chem. A 8 (2020) 6034–6040.

[26] J. Han, N.J. Li, D.Y. Chen, Q.F. Xu, J.M. Lu, Boosting photocatalytic activity for porphyrin-based D-A conjugated polymers via dual metallic sites regulation, Appl. Catal. B: Environ. 317 (2022), 121724.

[27] D. Feng, Z.Y. Gu, J.R. Li, H.L. Jiang, Z. Wei, H.C. Zhou, Zirconium-metalloporphyrin PCN-222: mesoporous metal-organic frameworks with ultrahigh stability as biomimetic catalysts, Angew. Chem. 124 (2012) 10453–10456.

[28] B.Y. Liu, J.Y. Du, G.L. Ke, B. Jia, Y.J. Huang, H.C. He, Y. Zhou, Z.G. Zou, Boosting O_2 reduction and H_2O dehydrogenation kinetics: surface n-hydroxymethylation of g-C_3N_4 photocatalysts for the efficient production of H_2O_2, Advanced Functional Materials, 32(15), 2111125.

[29] W.L. Sheng, X.X. Wang, Y.X. Wang, S.L. Chen, X.J. Lang, Integrating TEMPO into a Metal-Organic Framework for Cooperative Photocatalysis: Selective Aerobic Oxidation of Sulfides, ACS, Catalysis 12 (2022) 11078–11088.

[30] W. Wang, L. Bv, F. Tao, NiO/g-C_3N_4 composite for enhanced photocatalytic properties in the wastewater treatment, Environ. Sci. Pollut. Res. 30 (2023) 25620–25634.

[31] Y. Deng, J. Liu, Y. Huang, M. Ma, K. Liu, X. Dou, Z. Wang, S. Qu, Z. Wang, Engineering the Photocatalytic Behaviors of g-C_3N_4-based metal-free materials for degradation of a representative antibiotic, Adv. Funct. Mater. 30 (2020) 2002353.

[32] Y. Zhou, C. Zhang, D.L. Huang, W.J. Wang, Y.B. Zhai, Q.H. Liang, Y. Yang, S. H. Tian, H.Z. Luo, D.Y. Qin, Structure defined 2D Mo_2C/2D g-C_3N_4 Van der Waals heterojunction: Oriented charge flow in-plane and separation within the interface to collectively promote photocatalytic degradation of pharmaceutical and personal care products, Appl. Catal. B: Environ. 301 (2022), 120749.

[33] Y. Li, Y. Fang, Z. Cao, N. Li, D. Chen, Q. Xu, J. Lu, Construction of g-C_3N_4/PDI@ MOF heterojunctions for the highly efficient visible light-driven degradation of pharmaceutical and phenolic micropollutants, Appl. Catal. B: Environ. 250 (2019) 150–162.

[34] R. Chen, Y. Wang, Y. Ma, A. Mal, X.-Y. Gao, L. Gao, L. Qiao, X.-B. Li, L.-Z. Wu, C. Wang, Rational design of isostructural 2D porphyrin-based covalent organic frameworks for tunable photocatalytic hydrogen evolution, Nature, Communications 12 (2021) 1354.

[35] H.J. Jia, D.X. Ma, S.W. Zhong, L.J. Li, L. Li, L. Xu, B.Y. Li, Boosting photocatalytic activity under visible-light by creation of PCN-222/g-C_3N_4 heterojunctions, Chem. Eng. J. 368 (2019) 165–174.

[36] H.M. He, H.K. Li, Q.Q. Zhu, C.P. Li, Z.H. Zhang, M. Du, Hydrophobicity modulation on a ferriporphyrin-based metal-organic framework for enhanced ambient electrocatalytic nitrogen fixation, Appl. Catal. B: Environ. 316 (2022), 121673.

[37] D. Zhou, J. Zhang, Z. Jin, T. Di, T. Wang, Reduced graphene oxide assisted g-C_3N_4/rGO/NiAl-LDHs type II heterostructure with high performance photocatalytic CO_2 reduction, Chem. Eng. J. 450 (2022), 138108.

[38] S. Shao, J. Zhang, L. Li, Y. Qin, Z.-Q. Liu, T. Wang, Visible-light-driven photocatalytic N_2 fixation to nitrates by 2D/2D ultrathin $BiVO_4$ nanosheet/rGO nanocomposites, Chem. Commun. 58 (2022) 2184–2187.

[39] Q. Zhang, S. Huang, J. Deng, D.T. Gangadharan, F. Yang, Z. Xu, G. Giorgi, M. Palummo, M. Chaker, D. Ma, Ice-Assisted Synthesis of Black Phosphorus nanosheets as a metal-free photocatalyst: 2D/2D heterostructure for broadband H_2 evolution, Adv. Funct. Mater. 29 (2019), 1902486.

[40] S. Daliran, M. Khajeh, A.R. Oveisi, J. Albero, H. Garcia, $CsCu_2I_3$ Nanoparticles incorporated within a mesoporous metal-organic porphyrin framework as a catalyst for one-pot click cycloaddition and oxidation/knoevenagel tandem reaction, ACS Appl. Mater. Interfaces 14 (2022) 36515–36526.

[41] Q. Liu, Y. Guo, Z. Chen, Z. Zhang, X. Fang, Constructing a novel ternary Fe(III)/graphene/g-C_3N_4 composite photocatalyst with enhanced visible-light driven photocatalytic activity via interfacial charge transfer effect, Appl. Catal. B: Environ. 183 (2016) 231–241.

[42] X. Li, Y. Pi, Q. Xia, Z. Li, J. Xiao, $TiO2$ encapsulated in Salicylaldehyde-NH2-MIL-101(Cr) for enhanced visible light-driven photodegradation of MB, Appl. Catal. B: Environ. 191 (2016) 192–201.

[43] N. Geng, W. Chen, H. Xu, M. Ding, T. Lin, Q. Wu, L. Zhang, Insights into the novel application of Fe-MOFs in ultrasound-assisted heterogeneous Fenton system: Efficiency, kinetics and mechanism, Ultrason. Sonochem. 72 (2021) 105411.

[44] R.D. Tang, D.X. Gong, Y.Y. Zhou, Y.C. Deng, C.Y. Feng, S. Xiong, Y. Huang, G. W. Peng, L. Li, Unique g-C$_3$N$_4$/PDI-g-C$_3$N$_4$ homojunction with synergistic piezo-photocatalytic effect for aquatic contaminant control and H$_2$O$_2$ generation under visible light, Appl. Catal. B: Environ. 303 (2022), 120929.

[45] H. Liu, H. Yin, X. Yu, M. Zhu, Z. Dang, Amino-functionalized MIL-88B as heterogeneous photo-Fenton catalysts for enhancing tris-(2-chloroisopropyl) phosphate (TCPP) degradation: Dual excitation pathways accelerate the conversion of FeIII to FeII under visible light irradiation, J. Hazard. Mater. 425 (2022), 127782.

[46] P.M. Stanley, K. Hemmer, M. Hegelmann, A. Schulz, M. Park, M. Elsner, M. Cokoja, J. Warnan, Topology- and wavelength-governed CO$_2$ reduction photocatalysis in molecular catalyst-metal-organic framework assemblies, Chem. Sci. 13 (2022) 12164–12174.

[47] K. Yang, J. Ye, Y. Zhao, K. Ge, J.Y. Cao, S. Wang, Z.H. Zhang, Y. Zhang, Y.F. Yang, IO-TiO$_2$/PCN-222 Heterostructure with a Tightly Connected Interface and Its Photocatalytic Activity, Chemistryselect 6 (2021) 4238–4246.

[48] P. Hu, G. Liang, B. Zhu, W. Macyk, J. Yu, F. Xu, Highly Selective Photoconversion of CO$_2$ to CH$_4$ over SnO$_2$/Cs$_3$Bi$_2$Br$_9$ Heterojunctions Assisted by S-Scheme Charge Separation, ACS Catal. (2023) 12623–12633.

[49] S. Wang, B. Jiang, J. Henzie, F. Xu, C. Liu, X. Meng, S. Zou, H. Song, Y. Pan, H. Li, J. Yu, H. Chen, J. Ye, Designing reliable and accurate isotope-tracer experiments for CO$_2$ photoreduction, Nature, Communications 14 (2023) 2534.

[50] C. Wang, A. Mirzaei, Y. Wang, M. Chaker, Q. Zhang, D. Ma, BiVO$_4$ microspheres coated with nanometer-thick porous TiO$_2$ shells for photocatalytic water treatment under visible-light irradiation, ACS Appl. Nano Mater. 6 (2023) 5545–5556.

[51] H. Li, S. Tao, S. Wan, G. Qiu, Q. Long, J. Yu, S. Cao, S-scheme heterojunction of ZnCdS nanospheres and dibenzothiophene modified graphite carbon nitride for enhanced H$_2$ production, Chin. J. Catal. 46 (2023) 167–176.

[52] D. Zhou, S. Shao, X. Zhang, T. Di, J. Zhang, T. Wang, C. Wang, Construction of a 2D layered BiVO$_4$/zinc porphyrin (ZnTCPP) S-scheme heterostructure boosting photocatalytic N$_2$ oxidation performance, J. Mater. Chem. A 11 (2023) 401–407.

[53] Y. Wang, W. Cheng, P. Yuan, G. Yang, S. Mu, J. Liang, H. Xia, K. Guo, M. Liu, S. Zhao, G. Qu, B.-A. Lu, Y. Hu, J. Hu, J.-N. Zhang, Boosting nitrogen reduction to ammonia on FeN4 sites by atomic spin regulation, Advanced, Science 8 (2021), 2102915.

[54] Z. Li, Z. Zhuang, F. Lv, H. Zhu, L. Zhou, M. Luo, J. Zhu, Z. Lang, S. Feng, W. Chen, L. Mai, S. Guo, The marriage of the FeN4 moiety and mxene boosts oxygen reduction catalysis: Fe 3d electron delocalization matters, Adv. Mater. 30 (2018), 1803220.

[55] Y.K. Dai, B. Liu, Z.Y. Zhang, P. Guo, C. Liu, Y.L. Zhang, L. Zhao, Z.B. Wang, Tailoring the d-Orbital splitting manner of single atomic sites for enhanced oxygen reduction, Adv. Mater. 35 (2023), 2210757.

[56] S. Chen, X. Liang, S. Hu, X. Li, G. Zhang, S. Wang, L. Ma, C.-M.L. Wu, C. Zhi, J. A. Zapien, Inducing Fe 3d electron delocalization and spin-state transition of fen4 species boosts oxygen reduction reaction for wearable zinc-air battery, Nano-Micro Lett. 15 (2023) 47.